Nanoscale

PAPER

View Article Online
View Journal | View Issue

Cite this: *Nanoscale*, 2024, **16**, 20955

Exploring nitrogen-mediated effects on Fe and Cu cluster development in graphene: a DFT study†

L. A. Alvarado-Leal,*[a] J. I. Paez-Ornelas,*[b] M. A. Ruiz-Robles,[a] J. Guerrero-Sánchez,[b] J. M. Romo-Herrera,*[b] H. N. Fernández-Escamilla,[a] Noboru Takeuchi[b] and E. G. Perez-Tijerina[a]

The controlled growth and stability of transition metal clusters on N-doped materials have become the subject of intense investigation for unveiling comprehension on the cluster growth evolution. In this study, we investigated the growth mechanisms of non-magnetic (copper) and magnetic (iron) clusters on graphene with two atomic vacancies, with and without pyridinic nitrogen (N). Our results determine the role of pyridinic N in the growth and physicochemical properties of the mentioned metal clusters. In an N environment, Cu grows perpendicularly, whereas under N-deficient conditions, the clusters agglomerate. Fe cumulate-type clusters are formed regardless of the presence of N. However, N causes the Fe clusters to rise over one side of the surface without deforming the monolayer; meanwhile, in the absence of N, the Fe clusters protrude from both sides of the monolayer. Remarkably, the presence of N makes it feasible to induce magnetization in the Cu_n–N_4V_2 systems and aid in focalizing the magnetic properties on the Fe clusters for the Fe_n–N_4V_2 case. These findings offer insights into the role of N in cluster growth, with potential implications for diverse applications, including magnetic and electrocatalytic materials.

Received 30th June 2024,
Accepted 27th September 2024

DOI: 10.1039/d4nr02713b

rsc.li/nanoscale

1. Introduction

In recent years, the integration of graphene and transition metals has emerged as a promising route in materials science, offering unique opportunities for tailoring electronic, magnetic, and catalytic properties at the nanoscale.[1,2] In particular, the controlled growth and stability of transition metal clusters on graphene surfaces have become the subject of intense investigation.[3,4]

Recent studies have demonstrated that when small groups of Ni, Pd, and Pt atoms are adsorbed on a graphene layer, they generally retain the structural characteristics of gas-phase atomic groups.[5,6] However, the strength of their interaction weakens as the size of the metal groups increases.[5–8] Moreover, researchers have explored the adsorption of transition metal atoms on graphene to modify their electronic, magnetic, and surface reactivity properties. This exploration holds significant implications in diverse fields, including spintronics, nanomagnetism, data storage, and catalysis.[9–12]

Parallel investigations have scrutinized the interactions between metal clusters and graphene sheets, revealing that interfacial energy substantially influences the stability of these metal/graphene systems.[13] Similar interaction energies are observed for specific cluster sizes, even when oriented differently upon contact with the graphene material.[13] Another research strand is the potential of employing diverse defective graphene sheets to support transition metals.[14] It was observed that metals form stronger bonds with defective graphene, thereby contributing to their stabilization without significantly compromising the magnetic properties. Notably, magnetic anisotropy is boosted substantially when certain metals are deposited on defective graphene despite the intrinsic non-magnetic nature of carbon.[15,16]

Recent density functional theory studies have advanced our understanding of the structural, electronic, and magnetic properties of small transition metal clusters. For iron clusters (Fe_n, $n \leq 17$), significant findings include "magic numbers" at specific sizes (n = 6, 8, 10, 13, and 15) and noncollinear magnetic structures influenced by the Jahn–Teller effect, revealing high magnetic moments across varying configurations. The chemical reactivity of these clusters is primarily influenced by the coordination of individual atoms, and the addition of cobalt (Co) has been shown to enhance magnetic properties through structural rearrangements, providing insights into potential catalytic and magnetic applications.[17–20] Additionally, studies on small copper clusters (Cu_n, $n \leq 15$)

[a]*CICFIM Facultad de Ciencias Físico Matemáticas, Universidad Autónoma de Nuevo León, San Nicolás de los Garza, Nuevo León, Código Postal 66450, Mexico. E-mail: luis.alvaradoll@uanl.edu.mx, jmromo.at.ens.cnyn.unam.mx*
[b]*Centro de Nanociencias y Nanotecnología, Universidad Nacional Autónoma de México, Apartado Postal 14, Ensenada Baja California, Código Postal 22800, Mexico*
† Electronic supplementary information (ESI) available. See DOI: https://doi.org/10.1039/d4nr02713b

have demonstrated a preference for compact structures and identified unique growth pathways such as triangular and pentagonal bipyramidal arrangements. Furthermore, copper clusters on graphene quantum dots (GQDs) exhibit enhanced binding energy and conductivity, particularly when vacancies are present in graphene, highlighting new strategies for catalytic applications.[21,22]

Multiple variables, including the chemical environment, can impact the incorporation or growth of metals on the graphene network. These variables must be carefully analyzed to determine the factors that could favor or disfavor the process to obtain the desired metal/graphene system. Whether by cluster aggregation or growth, from the design of a single-atom catalyst (SAC) to a specific (few atoms) cluster, the process must be controllable and reproducible.

The performance of metallic SACs can be adversely affected by a considerable increase in the size of metal clusters and increased surface roughness, leading to a decrease in efficiency.[23–25] The primary objectives when trying to synthesize metallic SACs are high dispersion of individual atoms on suitable supports, *i.e.*, graphitic surfaces,[26–29] and reduction of contamination due to byproducts during synthesis. The most reasonable option to conduct experimental investigations on metallic SACs is the vacuum deposition method due to its good control over cluster size[30,31] and non-byproduct formation during synthesis. Therefore, this is a great opportunity for synthesis methods employing mass-selected and soft-landing techniques[32–35] in combination with magnetron sputtering[36] or inert gas condensation[37–39] due to their high atomic dispersion on substrates,[40] highly controlled cluster size,[41,42] and exceptionally low contamination compared with chemical methods that utilize molecules as stabilizers and chemical reactants as precursors of metallic atoms,[43] such as iron (Fe) single atoms and clusters.[44–48]

The incorporation of nitrogen into the carbon lattice has been widely explored for many reasons, such as modifying graphene's electronic properties and enabling fine-tuning of its electrical conductivity.[49,50] It is reported that nitrogen stabilizes carbon lattices with atomic vacancies or structural deformations. N-doped systems, such as N-doped nanotubes, are also widely applied in catalytic reactions.[51,52] Furthermore, nitrogen can facilitate strong interactions with transition metal atoms, potentially influencing cluster nucleation and growth.[53,54] Recent studies have shown that N-doped graphene-supported clusters, such as $Fe_3@N_4C_{16}$, exhibit enhanced electrocatalytic performance in the electrochemical nitrogen reduction reaction (eNRR) due to the modulation of the local electronic environment by nitrogen coordination.[55]

Transition metal single-atom catalysts (SACs) and clusters supported on graphene have demonstrated exceptional catalytic activity in various chemical reactions, and the ability to control their formation and stability through nitrogen doping can open new avenues for designing efficient catalysts.[56–58] In this study, we employed density functional theory (DFT) calculations to explore the effects of nitrogen on the formation and stability of magnetic and non-magnetic clusters (Fe and Cu, respectively) on graphene substrates. Specifically, we investigated the cluster aggregation and growth mechanisms from one- to six-atom clusters at carbon vacancies with and without pyridinic nitrogen, shedding light on the underlying mechanisms and potential applications of these composite systems. The outcomes of this research could drive innovations in various fields, from catalysis to advanced electronic devices.

2. Methods

Spin-polarized DFT calculations were conducted using the Quantum ESPRESSO package.[59–61] We employed ultrasoft pseudopotentials with the GGA–PBE approach (Perdew, Burke, and Ernzerhof) for the exchange–correlation (XC) potential.[62] Additionally, we accounted for long-range dispersion-corrected van der Waals interactions utilizing the Grimme-D3 scheme.[63] Kinetic energy cutoffs were set at 30 Ry and 240 Ry for the wave function and charge density, respectively. In geometric optimization, a Γ-centered Monkhorst–Pack mesh with *k*-point grids of 3 × 3 × 1 was applied for Brillouin zone integrations and 9 × 9 × 1 for electronic analysis.[64] We included an empty space of 20 Å perpendicular to the monolayer to prevent self-interaction due to periodic boundary conditions. The investigation of cluster growth was carried out in a 5 × 5 periodicity supercell.

3. Results and discussion

3.1. Substrates models TM_0–N_xV_2

Structural deformations in the carbon lattice tend to favor the coalition between the carbon substrate and the metallic adatoms. It is reported in the literature that the graphene lattice with two continuous carbon vacancies induces a hole that traps a metal adatom and incorporates it into the graphene lattice, generating a single-atom catalyst (SAC) model.[52] Therefore, for the initial phase of this study, we optimized the unit cell of the graphene structure to construct two carbon substrates where the cluster would interact. The optimized lattice parameter is a_0 = 2.46 Å, in good agreement with the experimental value.[65] Next, two graphene (5 × 5) models were built. The first one contains only a double vacancy (see Fig. 1(a)), whereas for the second model, we employed a graphene monolayer with two carbon vacancies that contain four pyridinic nitrogen atoms substituting four carbon atoms surrounding the double vacancy (see Fig. 1(b)).

These configurations are denoted as TM_n–N_4V_2 and TM_n–N_0V_2, where TM = {Fe, Cu}, the index n in TM_n represents the number of transition metal (TM) atoms incorporated into the model (where n varies from 0 to 6), N_x denotes the number of incorporated pyridinic nitrogen atoms in the monolayer (in this case, four or zero), and V_2 stands for the count of vacancies within the graphene original lattice. We designate carbon atoms bonded to the TM as $C_{\alpha 1}$ and to N as $C_{\alpha 2}$, as illustrated in Fig. 1. Despite the disparity in nitrogen doping

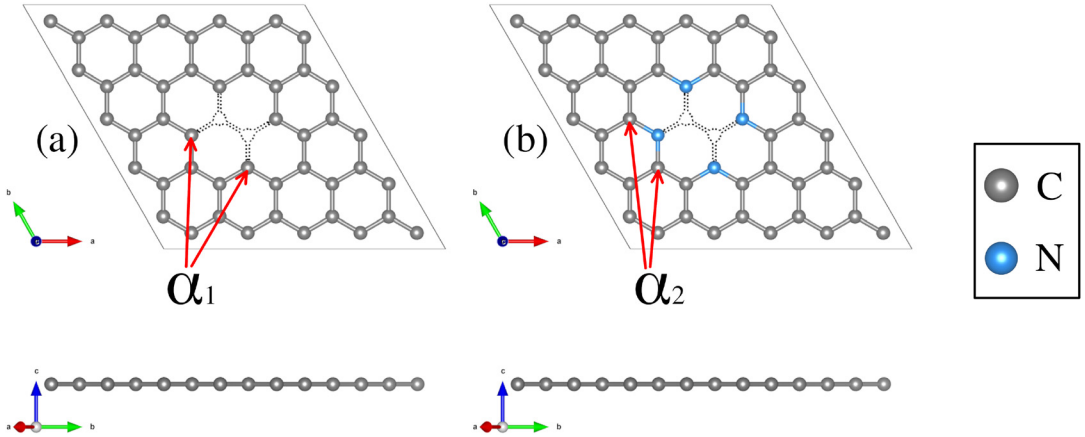

Fig. 1 Structural top and side views of (a) TM–N_0V_2 and (b) TM–N_4V_2. The C and N atoms are depicted as gray and blue spheres.

between both models, their structural resemblance is noteworthy, as both exhibit a planar structure, with C–C bond lengths of 1.42 Å and C–N bond lengths of 1.34 Å for the nitrogenated lattice.

Since both models contain different species around the vacancies where the TM atom is captured and incorporated into the lattice, we have characterized the charge distribution of the atoms around the vacancies of the clean substrates. To this end, we have employed the Bader charge (BC) formalism, which allows us to quantify the charge values associated with each atom.[66,67] The values obtained allow us to measure changes in the charge distribution ($\Delta Q = e_{\text{valence}} - \text{Bader}$) and provide vital information on the substrate–adsorbate interaction.

Regarding the charge distribution of the substrate models, an RGB color code has been employed to differentiate between charge loss, unchanged, and gain, respectively, depending on the ΔQ values. The charge redistribution is practically negligible when the system lacks N (see Fig. 2(a)). The slight variation of ΔQ in the TM_0–N_0V_2 model is around the carbon atoms of the vacancies due to the missing bonds. In contrast, for the TM_0–N_4V_2 model (see Fig. 2(b)), it is evident that the ΔQ values for the pyridinic nitrogen atoms indicate their role in inducing a redistribution of charge within the system due to the difference in electronegativity between the C and N atoms. The N atoms become charge acceptors, gaining an average of $-1.04e$. In contrast, the $C_{\alpha 2}$ atoms donate charge with an average value of $+0.52e$, while the remaining carbon atoms in the graphene lattice remain neutral.

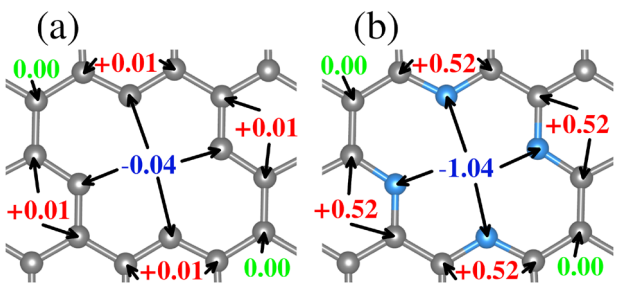

Fig. 2 Bader charges difference values per atom for the (a) TM_0–N_0V_2 system and (b) the TM_0–N_4V_2 system. An RGB color code was used to display the electronic charge loss (red), unchanged (green), or gained (blue).

3.2. Cluster formation in TM_n–N_xV_2 models

Once the TM_0–N_xV_2 substrates were structurally characterized, the systematic incorporation of Fe or Cu atoms, from one to six, in both monolayers was studied to delve into how the chemical environment of the substrate N or C_α atoms influences the TM_n adsorption states. This section thoroughly explores the one-by-one incorporation of TM_n atoms to form a cluster geometric shape. It describes their structural evolution during the growth stages, charge distribution, and magnetic and electronic properties as the TM_n cluster size increases. Furthermore, we do not combine TM species into the cluster. Fe and Cu elements were chosen due to their magnetic and non-magnetic characters in their corresponding bulk phases. However, the magnetic dipole moments in both TM_n clusters were explored due to their small cluster size.

3.2.1. Structural characterization of the cluster shape in TM_n–N_xV_2. Two substrate models have been selected, four systems were considered for systematically incorporating Fe and Cu atoms, each atom on TM_n–N_0V_2 and TM_n–N_4V_2. For the next part of the study, we refer to each adatom incorporation with the notation TM#1, where n ranges between one and six.

The first incorporation of the TM atom (TM#1) into both substrates (TM_1–N_xV_2) was favored at the C vacancies. These are the most favorable structural models for the initial TM adsorption, as depicted in Fig. 3(a-1), (b-1), (c-1), and (d-1) for Cu_1–N_4V_2, Cu_1–N_0V_2, Fe_1–N_4V_2, and Fe_1–N_0V_2, respectively, leading to a planar model with the formation of two pentagonal rings and two hexagonal rings (additional views of the adsorption states are shown in Fig. S1-1†).

For the next TM incorporation, the TM_2–N_xV_2 minimum energy models are illustrated in Fig. 3(a-2, b-2, c-2 and d-2). In

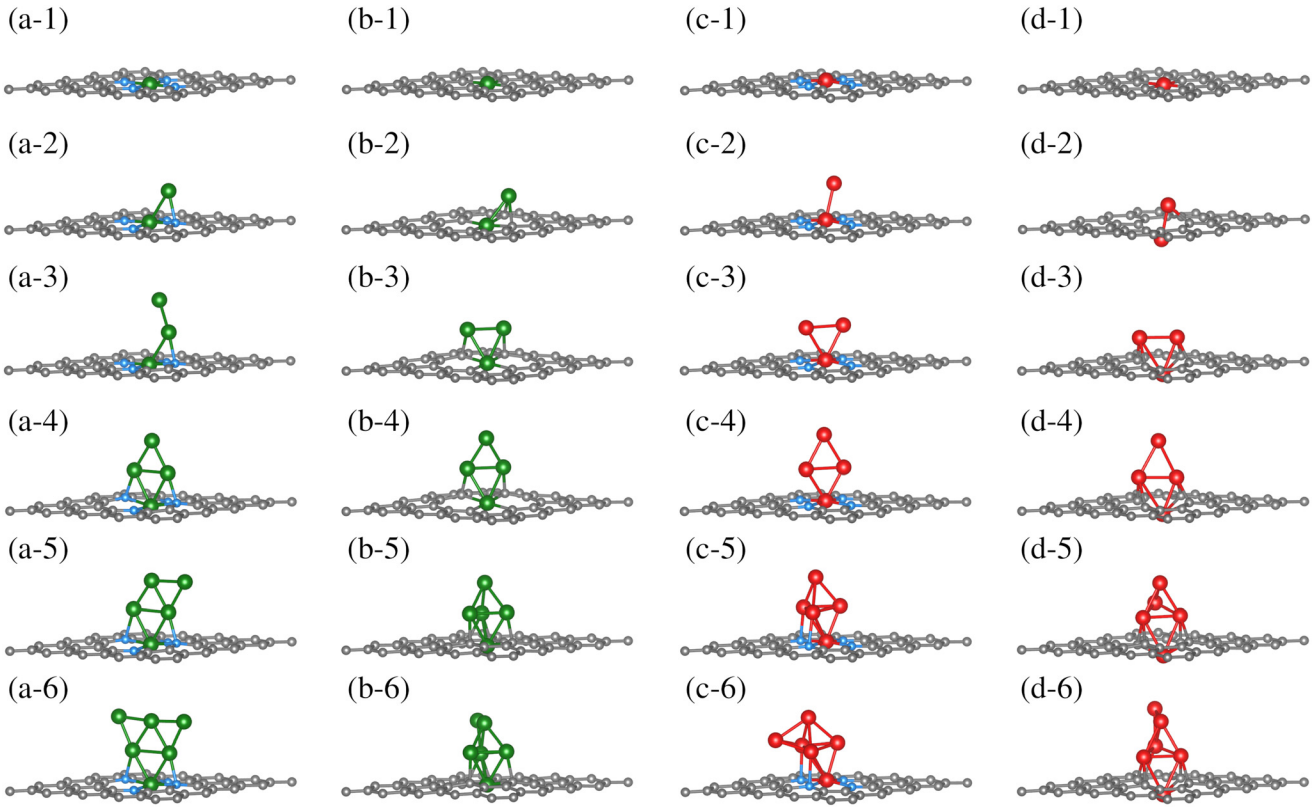

Fig. 3 Growth mechanism of clusters in the TM_n–N_xV_2 systems. The growth within the same system is observed horizontally, and the same growth stage is presented vertically for different systems. The C, N, Cu, and Fe atoms are depicted as dark, blue, green, and red spheres. For additional views of these configurations, refer to Fig. SI1.†

the case of Cu_2–N_4V_2, the second Cu atom (Cu#2) achieves a two-fold coordination with bonds to the first Cu atom (Cu#1) and to a neighboring N atom in a bridge-type position, as shown in Fig. 3(a-2). Meanwhile, in the Cu_2–N_0V_2 structure, Cu#2 is located over a hexagonal ring, reaching a three-fold coordination with Cu#1 and two $C_{\alpha1}$ atoms, as depicted in Fig. 3(b-2). In contrast, the Fe_2–N_4V_2 model's second Fe atom (Fe#2) does not form bonds with the lattice and remains in a top position above Fe#1, as shown in Fig. 3(c-2). Finally, in the Fe_2–N_0V_2 structure, a subtle deformation in the carbon system emerges; Fe#2 binds to two $C_{\alpha1}$ atoms, forming a hexagonal ring with the lattice and laying over the substrate. As a result, this model is no longer planar. Fe#2 bonds to Fe#1, driving it down the lattice and creating a symmetrical model. In this configuration, Fe#1 is now bonded to only two $C_{\alpha1}$ atoms, instead of four $C_{\alpha1}$ as in the TM_1–N_0V_2 model, as shown in Fig. 3(d-2). The Fe_2–N_0V_2 model does not present pentagonal rings since the Fe–Fe bond turns them into hexagonal non-planar rings (see Fig. S1-1†). Accordingly, there are already evident geometrical differences between the four TM_2–N_xV_2 models. The differences are influenced by a combination of factors. For example, in the case of the copper models (Cu_2–N_4V_2 and Cu_2–N_0V_2), the second copper atom can form different types of bonds depending on its local environment. This is because copper can have different oxidation states and coordination geometries, which influence how it bonds with neighboring nitrogen and carbon atoms. In contrast, in the iron models (Fe_2–N_4V_2 and Fe_2–N_0V_2), the second iron atom tends to maintain a higher position above the carbon substrate. This may be due to the unique magnetic and electronic properties of iron, which can influence its interaction with the carbon network and affect its ability to form bonds with other atoms. Additionally, differences in the structure of the models may be related to the availability of binding sites and the stability of the formed bonds. For instance, in the case of the Fe_2–N_0V_2 model, subtle deformation in the carbon network may be influenced by the interaction between the iron atoms and nearby carbon atoms, resulting in a more complex and non-planar structure.

The subsequent incorporation of TMs is related to the TM_n–N_xV_2 models. An open structure constitutes the most stable model for Cu#3 on TM_3–N_4V_2. Cu#3 only bonds with Cu#2, whereas the rest of the model remains unchanged, extending the Cu-cluster shape upward, as depicted in Fig. 3(a-3). On the other hand, Cu#3 in Cu_3–N_0V_2 forms three chemical bonds, binding with the pair of Cu atoms (Cu#1 and Cu#2) and a $C_{\alpha1}$. Moreover, the Cu#2 atom also reaches three-fold coordination. However, instead of being bound with two $C_{\alpha1}$ as in Cu_2–N_0V_2, it bounds to one $C_{\alpha1}$ and the other two Cu atoms, forming a triangular shape, as shown in Fig. 3(b-3).

The $C_{\alpha1}$ atoms bonded to Cu atoms are in the same pentagonal ring. The Fe_3–N_xV_2 model holds a triangular shape for the Fe atoms on both substrates. However, only Fe#1 is bonded to the four N atoms along the monolayer plane, while neither Fe#2 nor Fe#3 bonds to any substrate atom. In this configuration, the Fe_3 triangle cluster lies perpendicular to the substrate plane, positioning Fe#2 and Fe#3 over opposite hexagonal rings (Fig. 3(c-3)). On the other hand, in Fe_3–N_0V_2, since Fe#1 has crossed the substrate lattice, Fe#2 and Fe#3 bond to two $C_{\alpha1}$ each. Fe_3–N_0V_2 presents a more significant number of chemical bonds, as shown in Fig. 3(d-3). Furthermore, in Cu_3–N_0V_2, Fe_3–N_4V_2, and Fe_3–N_0V_2, the TM cluster shape induces a similar chemical environment for TM#2 and TM#3; that is to say, these are atoms with equivalent bond symmetries.

The fourth TM incorporation generates the TM_4–N_xV_2 models shown in Fig. 3(a-4, b-4, c-4 and d-4). Note that in the Cu_4–N_xV_2 model, three Cu atoms are chemically bonded to the substrate. On the nitrogenated substrate, Cu#1 bonds to all N atoms; Cu#2 and Cu#4 bond to an opposite N atom in Cu_4–N_4V_2 (Fig. 3(a-4)). Meanwhile, in Cu_4–N_0V_2, Cu#4 is the Cu atom that does not bind to the substrate (Fig. 3(b-4)), and as described in the Cu_3–N_0V_2 model, Cu#2 and Cu#3 bond to adjacent $C_{\alpha1}$ in a pentagonal ring. For Fe_4–N_4V_2, Fe#1 is still the only Fe atom of the Fe_4 cluster that is chemically bonded to the substrate; the other three Fe atoms bond only to Fe atoms, adopting a perpendicular planar configuration (Fig. 3(c-4)). On the other hand, in Fe_4–N_0V_2, Fe#4 is the only Fe atom that doesn't bond to the substrate, and the rest of the Fe atoms remain unchanged compared with the Fe_3–N_0V_2 model (Fig. 3(c-4)). The TM_4–N_xV_2 model form rhomboidal cluster shapes across the substrates except for Cu_4–N_0V_2, where the rhombohedral cluster shape is planar and perpendicular to the monolayer (see Fig. S1(a–d)4†). Additionally, the TM4 cluster induces an identical adsorption position for TM#2 and TM#3, generating a triangular configuration with TM#1.

The subsequent incorporation generates the TM_5–N_xV_2 models. For Cu#5 on the nitrogenated substrate (TM_5–N_4V_2), a semi-triangular cluster shape is generated where Cu#5 is two-fold coordinated with the Cu#4 atom and a Cu atom that interacts with an N atom from the substrate (Fig. 3(a-5)). For the TM_5–N_0V_2 substrate, the Cu#5 atom reaches a three-fold coordination with three Cu atoms, completing a rhombohedral shape (Fig. 3(b-5)). For the addition of Fe atoms, the Fe#5 atom also achieves a similar configuration to the previously described Cu#5 over the TM_5–N_4V_2 substrate, while on TM_5–N_0V_2 the same cluster shapes emerge. In this configurations, a pair of Fe atoms supporting the top Fe#5 atom of the rhombohedral cluster establishes an interaction with the surface.

Finally, we present the TM_6–N_xV_2 models. In the Cu_6–N_4V_2 model, the Cu_6 cluster maintains its planar arrangement, forming a planar triangular cluster. In the Cu_6–N_0V_2 model, Cu#6 bonds with two Cu atoms (Cu#4 and Cu#5) in a bridge position, as shown in Fig. 3(b-6). For the Fe_6–N_4V_2 model, Fe#6 bonds to three Fe atoms without interacting with the surface atoms, as shown in Fig. 3(c-6). Meanwhile, in the Fe_6–N_0V_2 model, Fe#6 similarly binds to the Fe cluster as Cu#6 does in forming the Cu_6 cluster. In addition, the optimized structures of free-standing Cu/Fe clusters, independent of the substrate, are provided in the ESI (S1).†

3.2.2. TM_n–N_xV_2 charge distribution. We analyzed the electronic charge distribution after describing the structural models of TM_n–N_xV_2. Bader difference charge calculation ΔQ, defined in section 4.1, was employed to comprehensively understand charge distribution throughout the cluster size increment in the TM_n–N_xV_2 models. The calculated ΔQ values per TM atom for the different cluster sizes are depicted in Fig. 4. The RGB color codes employed are red, green, and blue for charge loss, unchanged, and gain.

All TMs display charge loss upon joining the substrate for the first TM incorporation. Notably, a discernible trend exists where TM#1 tends to lose more electronic charge in a nitrogen-rich environment. This trend is primarily attributed to nitrogen's role as a charge acceptor, as shown in the first row of Fig. 4. On the nitrogenated substrates, Cu loses +0.93*e* while Fe loses +1.18*e*; on the TM_1–N_0V_2 substrate the values are +0.65*e* and +0.98*e* for Cu and Fe.

In contrast to TM_1–N_xV_2, in the TM_2–N_xV_2 models, TM#1 reduces its charge donation value to the substrate, and in all cases, TM#2 also shows an electronic donor charge character. As described in the structural characterization of the cluster shape in TM_n–N_xV_2 section, since the TM#2 chemical environment is distinct in each TM_2–N_xV_2 model, TM#2 yields different amounts of charge. In Cu_2–N_4V_2, Cu#2 (bonded to Cu#1 and a N atom) gives +0.14*e*, in addition to the +0.86*e* provided by Cu#1, resulting in the entire Cu_2 cluster giving +1.00*e* to the substrate (see Fig. 4(a-2)). Meanwhile, in Cu_2–N_0V_2, Cu#2 (bonded to Cu#1 and two $C_{\alpha1}$) yields +0.46*e* and Cu#1 yields +0.61*e*. Hence, the Cu_2 cluster gives a total of +1.07*e* to the substrate (see Fig. 4(b-2)). In Fe_2–N_4V_2, Fe#1 and Fe#2 provide +0.99*e* and +0.26*e*, respectively, as shown in Fig. 4(c-2); therefore, the Fe_2 cluster yields +1.25*e* to the substrate. In Fe_2–N_0V_2, the Fe_2 cluster yields +1.61*e*; since both Fe atoms have a similar chemical environment, the calculated ΔQ for each Fe atom is almost identical (see Fig. 4(d-2)). All the calculated ΔQ values per TM atom and the clusters' ΔQ values are shown in Fig. 4.

The clusters composed by a third TM atom (TM_3–N_xV_2) present a donor charge character except for the Cu_3–N_4V_2 model where the third adatom presents an electron gain value of −0.16*e*, and the previous adatoms had values +0.19*e* and +0.89*e*. Note that the coordination of this atom is single-bonded with the previous Cu atom. In contrast, for the other TM_3–N_xV_2 models, the incorporated atoms are two-fold coordinated with the previous TM atoms, and interaction with the substrate for the second and third TM is also evident for the substrates without N. The total cluster charge values are +0.92, +1.07, +1.50, and +1.87 for Cu_3–N_4V_2, Cu_3–N_0V_2, Fe_3–N_4V_2, and Fe_3–N_0V_2, respectively (see Fig. 4(a-d3)).

With the fourth TM incorporation and the formation of a planar cluster for the studied models, the TM#4 atom does not interact with the substrate. It is only two-fold coordinated with the contiguous TM atoms, presenting a charge acceptor char-

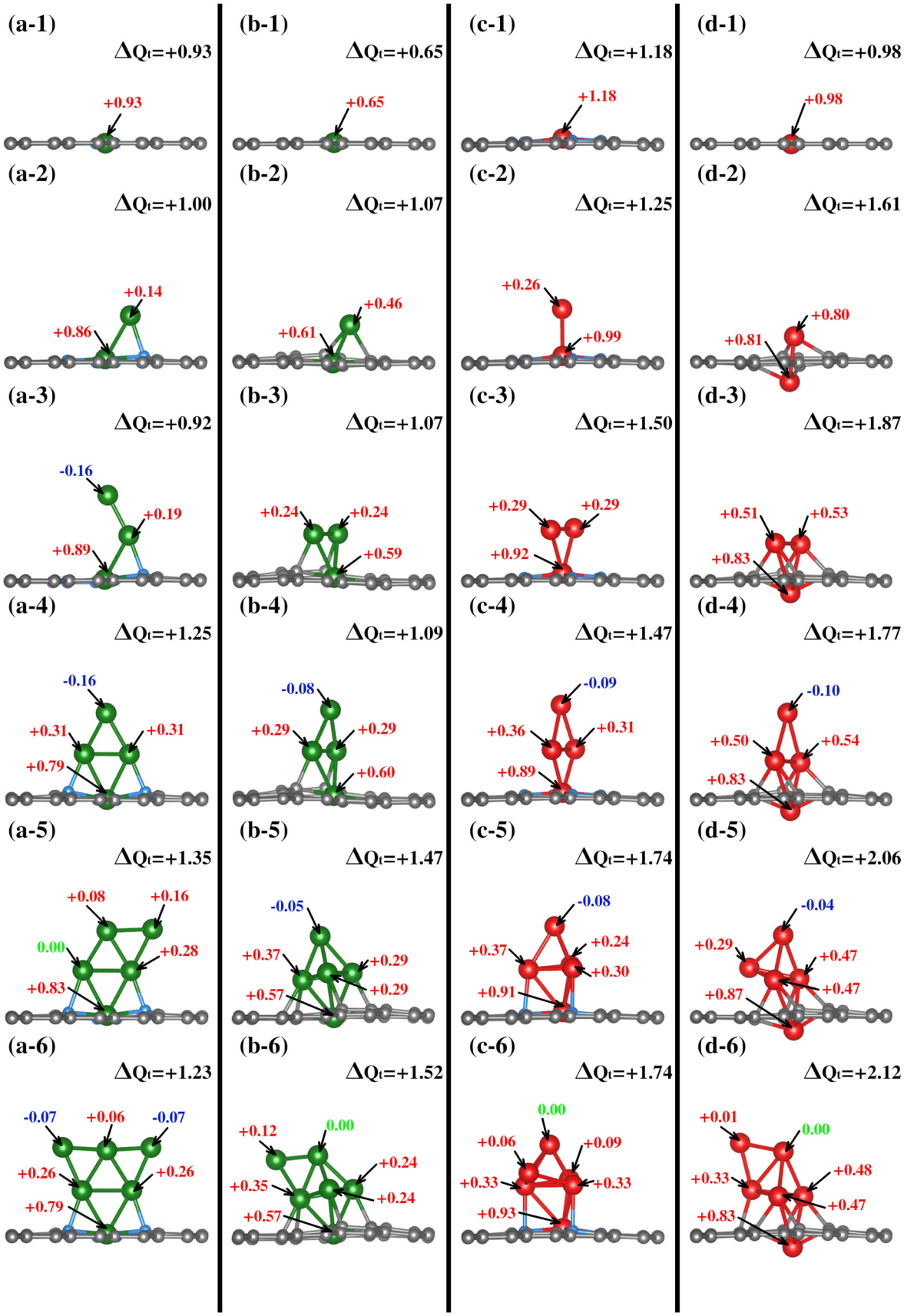

Fig. 4 Bader charges monitored throughout the growth mechanism of each system, with each row corresponding to the same state observed in different systems and each column depicting the growth pathway for a specific system.

acter. For Cu_4–N_4V_2 (Fig. 4(a-4)), the charge values are −0.16*e*, +0.31*e*, +0.31*e*, and +0.79*e*, providing a total cluster charge of +1.25*e*. In Cu_4–N_0V_2, the same trend appears with charge values of −0.08*e*, +0.29*e*, +0.29*e*, and +0.60*e* for a total of +1.1*e* for the complete cluster. The same trend is observed for the Fe cluster, where the Fe atoms had charge values of −0.09*e* and −0.10*e* for Fe_4–N_4V_2 and Fe_4–N_0V_2. Accordingly, the cluster charge values are +1.25, +1.09, +1.47, and +1.77. In this case, although the TM#4 atom accepts a minimal charge, its role as an acceptor suggests a unique dynamic in the system. This is due to its position and interactions with neighboring atoms, where factors like low electron density and electrostatic forces may have an influence. Such behavior underscores the complexity of these systems, where slight variations have significant impacts on their behavior and properties.

The subsequent incorporation of atoms generates the TM#5 models, except for the semi triangular Cu_5–N_4V_2 cluster, where the added Cu atom acts as a charge donor with a value of +0.16*e*, the rhombohedral clusters with the TM at the tip present a ΔQ gain of −0.05*e*, −0.08*e* and −0.04*e* for Cu_5–N_0V_2, Fe_5–N_4V_2, and Fe_5–N_0V_2, respectively. The cluster charge values are +1.35, +1.47, +1.74, and +2.06.

Finally, for the clusters formed by six atoms, it is observed that the triangular planar cluster has a charge acceptor character at the edges, two-fold coordinated Cu atoms, with values of −0.07*e*. The remaining systems, which form rhombohedral clusters, show a TM with unchanged charge $\Delta Q = 0$. The total charge migration values are +1.23, +1.52, +1.74, and +2.21 for Cu_6–N_4V_2, Cu_6–N_0V_2, Fe_6–N_4V_2, and Fe_6–N_0V_2, respectively.

Overall, throughout the growth process, the TM_n cluster donates electronic charge to the substrates. Additionally, atoms within each TM_n cluster with equivalent chemical environments exhibit the same ΔQ value.

3.2.3. TM_n–N_xV_2 magnetic properties. For a better understanding of the magnetic properties throughout the cluster growth, the magnetic moments of each atom in the TM_n–N_xV_2 systems were characterized, as shown in Fig. 5. Additionally, Table 1 presents the contributions to the total magnetization from both the cluster and the substrate.

Between the Cu–N_4V_2 and Cu–N_0V_2 systems, the main distinction lies in the total magnetization of the structure. In Cu–N_4V_2, there is consistently intrinsic magnetization in the system. In contrast, the Cu–N_0V_2 structures exhibit negligible magnetization throughout the cluster growth, as depicted in columns a and b of Fig. 5. This suggests that Cu in a nitrogen-free environment does not induce polarization in the substrate, unlike in an environment with nitrogen (refer to Table 1). Additionally, it is noteworthy that as the cluster grows in Cu–N_4V_2, the Cu atoms in the monolayer exhibits significant magnetic characteristics. This point is attributed to forming bonds with nitrogen, inducing a magnetic moment in Cu. This can be observed in Fig. 5(a-3), (a-4), (a-5), and (a-6), where the copper in the monolayer displays the highest magnetic moments of +0.43μ_B, +0.27μ_B, +0.36μ_B, and −0.31μ_B, respectively.

In the case of the Fe–N_xV_2 structures, Table 1 shows that in structures with N, the primary contribution to the total magnetization comes from the cluster, with minimal contribution from the substrate. This is attributed to Fe being inherently magnetic, and the presence of N does not significantly affect its polarization throughout the cluster growth. On the other hand, in the Fe–N_0V_2 structures, Table 1 suggests a more substantial contribution from the substrate, as observed in Fig. 5 (d-1). In this case, the substrate contributes +0.77μ_B, adding to the +1.30μ_B from Fe, resulting in a total magnetization of +2.07μ_B. It is noteworthy that, unlike iron, the presence of nitrogen is crucial for inducing polarization in the Cu species. This observation can be elucidated by considering the electronic and chemical interactions within the Cu–N systems. Cu is a transition metal with partially filled d-orbitals, making it inherently susceptible to magnetic moments. However, in the absence of specific external influences, the magnetic behavior of copper might remain relatively subdued. The introduction of nitrogen into the system creates a dynamic environment where the Cu atoms interact with the nitrogen atoms, forming Cu–N bonds. These bonds can introduce unpaired electrons and alter the electronic configuration of the Cu atoms. The interaction with nitrogen induces a magnetic polarization in the Cu species, enhancing its magnetic characteristics. In contrast, Fe is already a well-known magnetic species due to its intrinsic magnetic moments arising from its electron configuration. Therefore, in the Fe–N systems, the impact of nitrogen on iron magnetic behavior may be comparatively less pronounced. Fe's inherent magnetism is less influenced by nitrogen, resulting in a more consistent magnetic behavior throughout the cluster growth.

3.2.4. TM_n–N_xV_2 electronic properties. To enhance our comprehension of the electronic structure within each system, we have generated density of states plots of the entire growth mechanism, as illustrated in Fig. 6. In the case of the Cu–N_4V_2 system, as depicted in Fig. 6(a-1), it can be seen that in the vicinity of the Fermi level, the contributions of nitrogen coincide with those of copper, indicating the interaction between Cu and N. In the case of $2Cu_2$–N_4V_2, the Cu contributions intensify, exhibiting well-defined peaks at around −2 eV (Fig. 6(a-2)). As the cluster size increases, the Cu contributions continue to increase, providing evidence of an increased presence of Cu in the system and, consequently, a more pronounced interaction between the monolayer and the cluster.

In the case of Cu–N_0V_2, where nitrogen is absent, copper (Cu) exhibits contributions at the same energy level and slightly to the right (Fig. 6(b-1)). This observation indicates the stability that copper gains when it incorporates embedded nitrogen within the monolayer. As the cluster grows, the Cu contributions increase in intensity, consistently remaining at around −2 eV.

In the context of the Fe–N_4V_2 system, which is presented in Fig. 6(c-1), it is worth highlighting the position of the contributions in relation to the formation of N–Fe bonds. These contributions are observed at approximately 2 eV, which is slightly to the right compared to their counterparts in the case of copper (Cu). This difference in positioning suggests distinct

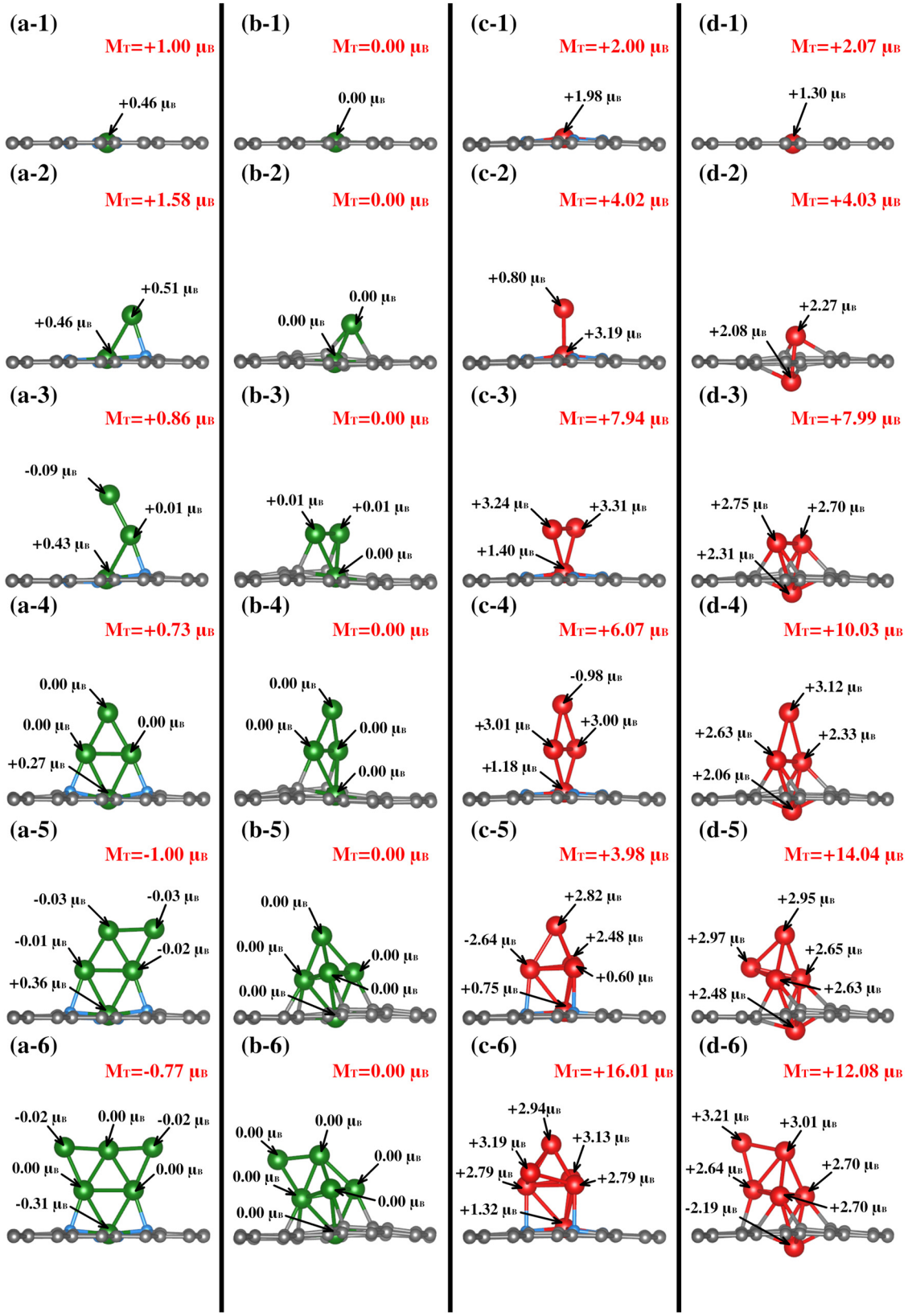

Fig. 5 Magnetic moments of each metal site for the TM_n–N_xV_2 systems. The total magnetization of each system is depicted in red. Panels (a)–(d) correspond to Cu–N_4V_2, Cu–N_0V_2, Fe–N_4V_2, and Fe–N_0V_2, respectively.

Table 1 Contribution to magnetization in each system. M_T denotes the total magnetization of the system, M_{Cl} represents the magnetization of the cluster, and M_{subs} stands for the magnetization associated with the substrate

	Cu–N_4V_2 (μ_B)			Cu–N_0V_2 (μ_B)			Fe–N_4V_2 (μ_B)			Fe–N_0V_2 (μ_B)		
System	M_T	M_{Cl}	M_{subs}	M_T	M_{Cl}	M_{subs}	M_T	M_{Cl}	M_{subs}	M_T	M_{Cl}	M_{subs}
TM_1	1.00	0.46	0.54	0.00	0.00	0.00	2.00	1.98	0.02	2.07	1.30	0.77
TM_2	1.58	0.98	0.60	0.00	0.00	0.00	4.02	4.00	0.02	4.03	4.36	−0.33
TM_3	0.86	0.34	0.52	0.00	0.00	0.00	7.94	7.97	−0.03	7.99	7.78	0.21
TM_4	0.73	0.28	0.45	0.00	0.00	0.00	6.07	6.22	0.14	10.03	10.16	−0.13
TM_5	−1.00	−0.48	−0.52	0.00	0.00	0.00	3.98	4.01	−0.03	14.04	13.71	0.34
TM_6	−0.77	−0.38	−0.38	0.00	0.00	0.00	16.01	16.19	−0.18	12.08	12.09	−0.01

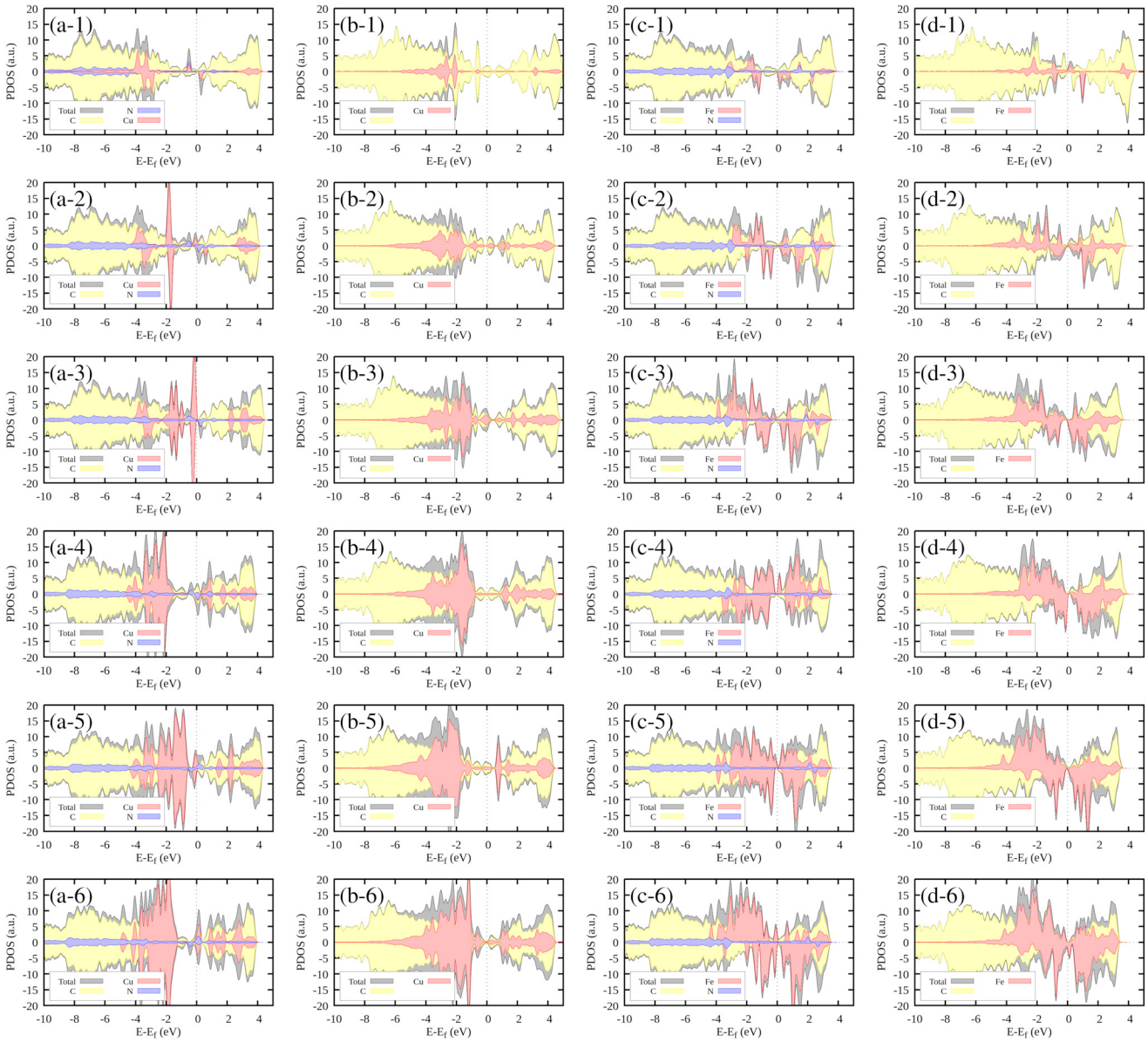

Fig. 6 Projected densities of states (PDOSs) for the (a) Cu–N_4V_2, (b) Cu–N_0V_2, (d) Fe–N_4V_2, and (e) Fe–N_0V_2 systems. The total system contribution is shown in black; the yellow segment represents the contribution from carbon (C) atoms and the blue component shows the contribution from nitrogen (N) atoms. The red segment corresponds to the transition metal (TM), which can be either copper (Cu) or iron (Fe).

energy requirements and behaviors for bond formation between nitrogen and iron as opposed to nitrogen and copper. Furthermore, as the cluster size increases, we notice an intriguing phenomenon. The intensity of the iron (Fe) contributions intensifies, indicating an enhanced presence of iron atoms in the system. However, this observation is particularly intriguing because these contributions do not maintain a uniform energy level. Instead, they are distributed at various energy levels, indicating a diverse range of bonding configurations or states within the growing cluster.

Finally, in the case of the Fe–N_0V_2 system (Fig. 6(d-1)), we can observe a similar trend to the previous scenario. The behavior of the Fe contributions manifests at varying energy levels, displaying significant asymmetry between the spin-up and spin-down states. This asymmetry in the energy distribution further underscores the intricate electronic properties of the growing cluster, shedding light on the complexity of the Fe–C interactions in the absence of nitrogen.

In Fig. S3-1 of the ESI,† the DOS contribution from the most exposed transition metal in the system is highlighted in green. Notably, the contributions closest to the Fermi level, indicative of electronic states readily available for interaction, predominantly originated by the most exposed TMs. This observation hints at the unique electronic influence exerted by the most exposed TM within the cluster. Its distinct positioning or bonding characteristics likely facilitate localized electronic interactions, resulting in the emergence of prominent electronic states near the Fermi level. These states, in turn, play a pivotal role in shaping the electronic properties of the entire system, particularly in the vicinity of the Fermi energy.

3.2.5. Growth and aggregation analysis of TM_n–N_xV_2. To gain a better understanding of cluster size with N-doped and non N-doped substrates, we utilized the formalism of growth and aggregation energies, as described by eqn (1) and (2), respectively. In this way, we focus on identifying the chemical environment that may promote TM clusters' dispersion, growth, or aggregation. This formalism is very important because its capability to quantitatively assess the energetic aspects of cluster formation and evolution, facilitating a rigorous analysis of the stability and kinetics of the cluster growth process.[68]

$$E_{\mathrm{grow}}\left[\frac{n}{n-1}\right] = [E(\mathrm{TM}_n/\mathrm{slab}) + E(\mathrm{slab})] - [E(\mathrm{TM}_{n-1}/\mathrm{slab}) + E(\mathrm{TM}_1/\mathrm{slab})] \quad (1)$$

$$E_{\mathrm{agg}}\frac{(n)}{n} = \frac{[E(\mathrm{TM}_n/\mathrm{slab}) + (n-1)E(\mathrm{slab}) - nE(\mathrm{TM}_1/\mathrm{slab})]}{n} \quad (2)$$

The E_{grow} and E_{agg} values denote the growth and aggregation energies, respectively. E_{grow} compares the TM_n cluster against TM_{n-1} with a dispersed TM to analyze the one-atom growth mechanism. Meanwhile, E_{agg} compares the TM_n clusters with the n-TM dispersed. As the equations are expressed, negative E_{grow} or E_{agg} values indicate a thermodynamically more favorable configuration. This means that growth or aggregations are viable, respectively. $E(\mathrm{TM}_n/\mathrm{slab})$ is the TM_n–N_xV_2 total energy and $E(\mathrm{slab})$ is the substrate energy.

We will first discuss the E_{grow} results. Regarding the growth energies, as depicted in Fig. 7(a), it is evident that in the initial step, all the TM_2–N_xV_2 systems exhibit positive growth energies. Physically, considering eqn (1), this means a greater likelihood of adatoms arriving at vacancies rather than cluster growth. In this case, the positive energy values indicate that the influx of adatoms favors the saturation of vacancies before cluster growth, a trend observed across all systems. If controllable incorporation of TMs into carbon substrates could be achieved through high vacuum synthesis methods like magnetron sputtering, inert gas condensation, and soft-landing techniques (as clarified in the Introduction section), then highly dispersed SACs could be obtained, provided that two carbon vacancies are present in the substrate. It is noteworthy that the Fe_2–N_0V_2 system has the lowest E_{grow} value of 0.21 eV. Meanwhile, the N-doped substrates present the highest E_{grow} values.

The cluster growth will only occur once the vacancies are filled with the first TM. From now on, we will consider TM_1–N_xV_2 as $E(\mathrm{slab})$ in eqn (1). Once the vacancies are saturated and more TMs are incorporated into the system, one-atom cluster growth becomes feasible for Cu regardless of the presence of nitrogen, as evidenced by the negative E_{grow} value. Meanwhile, Fe cluster growth is only viable in the nitrogenate substrate, since the E_{grow} value of Fe–N_0V_2 is positive.

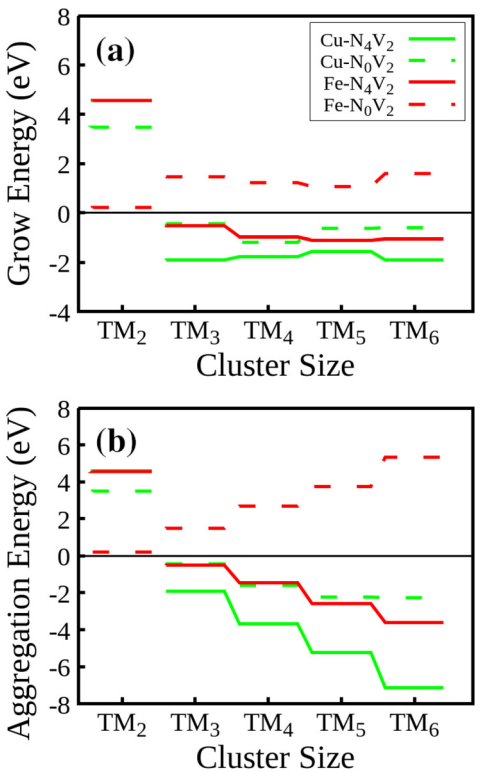

Fig. 7 (a) Growth energies and (b) aggregation energies for the TM–N_xV_2 structures during cluster formation.

In terms of the aggregation energies, as described by eqn (2) and illustrated in Fig. 7(b), we can observe that the E_{agg} values for clusters made of two atoms are positive. This observation confirms that it is imperative to first saturate the vacancies with a TM before cluster growth or aggregation in any system. Once this step is accomplished, the TM cluster aggregation becomes feasible for the Cu clusters on both substrates and the Fe cluster on the N-doped monolayer due to the negative value of E_{agg}.

These findings on aggregation and growth energies suggest that once all vacancies are saturated by a TM, a nitrogen-rich environment promotes the cluster growth mechanism, enabling systems to achieve increased stability as the growth process goes on. This observation aligns with findings in published studies that have highlighted the role of nitrogen in modulating the properties and chemical reactivity of materials.[51,55] Specifically, these studies have emphasized the influence of nitrogen on the selectivity of specific reactions, such as the oxygen reduction reaction (ORR), where the presence of nitrogen in nitrogen-doped graphitic carbon materials has been shown to affect the preferred reaction pathway.[51] This consistency among findings underscores the significance of nitrogen in materials engineering for specific applications in fields like energy and the environment.

4. Conclusions

In this study, we investigated the growth mechanism of Cu and Fe clusters on a graphene monolayer, particularly examining scenarios with and without nitrogen doping (TM_n–N_xV_2). Our analysis reveals intriguing growth patterns, especially within Cu-based systems. The presence of pyridine nitrogen induces a more structured and orderly growth of Cu clusters, forming a stable plane perpendicular to the monolayer. In contrast, in nitrogen-deficient environments, Cu clusters exhibit less organized, more clumped formations.

Pyridine nitrogen also plays a crucial role in improving the structural stability of Fe clusters, reducing the deformations often observed in its absence. Additionally, nitrogen facilitates magnetization in Cu_n–N_4V_2 systems and focuses the magnetic properties in Fe clusters.

Using the formalism of aggregation and growth energies, we explored system stability, highlighting nitrogen as a key factor in enhancing stability, particularly favoring Cu cluster growth. Notably, as the cluster size increases, this stabilizing effect diminishes, suggesting a transition towards bulk-like behavior similar to Fe. These findings provide a deeper understanding on how pyridine nitrogen affects growth dynamics and catalytic properties, offering valuable insights for designing electrocatalysts. Understanding the minimum cluster size before transitioning to metallic behavior, similar to bulk iron, is crucial for influencing material reactivity and catalytic properties. These insights are essential for tailoring materials for improved electrocatalytic performance, with applications ranging from renewable energy generation to environmental cleanup.

Data availability

The data supporting this article have been included as part of the ESI.† For any further details please do not hesitate contacting us (jmromo@ens.cnyn.unam.mx or luis.alvaradoll@uanl.edu.mx).

Conflicts of interest

There are no conflicts to declare.

Acknowledgements

The authors acknowledge the financial support provided through DGAPA-UNAM with projects IN102725, IN111223, IG101124, and IN105722. Calculations were performed in the DGTIC-UNAM Supercomputing Center projects LANCAD-UNAM-DGTIC-051, LANCAD-UNAM-DGTIC-382, and LANCAD-UNAM-DGTIC-368. J. I. P. O. thanks DGAPA-UNAM for a postdoctoral position.

References

1 Y. Tang, Z. Yang and X. Dai, Trapping of metal atoms in the defects on graphene, *J. Chem. Phys.*, 2011, **135**, 224704.
2 B. Chai, T. Peng, J. Mao, K. Li and L. Zan, Graphitic carbon nitride (g-C3N4)-Pt-TiO2 nanocomposite as an efficient photocatalyst for hydrogen production under visible light irradiation, *Phys. Chem. Chem. Phys.*, 2012, **14**, 16745–16752.
3 Y.-H. Zhang, *et al.*, Tuning the magnetic and transport property of graphene with Ti atom and cluster, *Comput. Mater. Sci.*, 2012, **56**, 95–99.
4 O. Üzengi Aktürk and M. Tomak, Au_nPt_n clusters adsorbed on graphene studied by first-principles calculations, *Phys. Rev. B: Condens. Matter Mater. Phys.*, 2009, **80**, 085417.
5 C. R. C. Rêgo, P. Tereshchuk, L. N. Oliveira and J. L. F. Da Silva, Graphene-supported small transition-metal clusters: A density functional theory investigation within van der Waals corrections, *Phys. Rev. B*, 2017, **95**, 235422.
6 E. Yoo, *et al.*, Enhanced Electrocatalytic Activity of Pt Subnanoclusters on Graphene Nanosheet Surface, *Nano Lett.*, 2009, **9**, 2255–2259.
7 H. Yan, *et al.*, Single-Atom Pd1/Graphene Catalyst Achieved by Atomic Layer Deposition: Remarkable Performance in Selective Hydrogenation of 1, 3–1Butadiene, *J. Am. Chem. Soc.*, 2015, **137**, 10484–10487.
8 R. Hussain, *et al.*, Density functional theory study of palladium cluster adsorption on a graphene support, *RSC Adv.*, 2020, **10**, 20595–20607.
9 M. Manadé, F. Viñes and F. Illas, Transition metal adatoms on graphene: A systematic density functional study, *Carbon*, 2015, **95**, 525–534.

10 M. P. Lima, A. J. R. da Silva and A. Fazzio, Adatoms in graphene as a source of current polarization: Role of the local magnetic moment, *Phys. Rev. B: Condens. Matter Mater. Phys.*, 2011, **84**, 245411.
11 C. M. Acosta, M. P. Lima, R. H. Miwa, A. J. R. da Silva and A. Fazzio, Topological phases in triangular lattices of Ru adsorbed on graphene: Ab initio calculations, *Phys. Rev. B: Condens. Matter Mater. Phys.*, 2014, **89**, 155438.
12 X.-Q. Dai, Y.-N. Tang, J.-H. Zhao and Y.-W. Dai, Absorption of Pt clusters and the induced magnetic properties of graphene, *J. Phys.: Condens. Matter*, 2010, **22**, 316005.
13 K. Okazaki-Maeda, Y. Morikawa, S. Tanaka and M. Kohyama, Structures of Pt clusters on graphene by first-principles calculations, *Surf. Sci.*, 2010, **604**, 144–154.
14 S. Sahoo, M. E. Gruner, S. N. Khanna and P. Entel, First-principles studies on graphene-supported transition metal clusters, *J. Chem. Phys.*, 2014, **141**(7), 074707.
15 H. Johll, J. Wu, S. W. Ong, H. C. Kang and E. S. Tok, Graphene-adsorbed Fe, Co, and Ni trimers and tetramers: Structure, stability, and magnetic moment, *Phys. Rev. B: Condens. Matter Mater. Phys.*, 2011, **83**(20), 205408.
16 R. C. Longo, J. Carrete, J. Ferrer and L. J. Gallego, Structural, magnetic, and electronic properties of Ni_n and Fe_n nanostructures (n=1–4) adsorbed on zigzag graphene nanoribbons, *Phys. Rev. B: Condens. Matter Mater. Phys.*, 2010, **81**, 115418.
17 O. Diéguez, M. M. G. Alemany, C. Rey, P. Ordejón and L. J. Gallego, Density-functional calculations of the structures, binding energies, and magnetic moments of Fe clusters with 2 to 17 atoms, *Phys. Rev. B: Condens. Matter Mater. Phys.*, 2001, **63**(20), 205407.
18 J. Berwanger, S. Polesya, S. Mankovsky, H. Ebert and F. J. Giessibl, Atomically Resolved Chemical Reactivity of Small Fe Clusters, *Phys. Rev. Lett.*, 2020, **124**(9), 096001.
19 Q.-M. Ma, Z. Xie, J. Wang, Y. Liu and Y.-C. Li, Structures, binding energies and magnetic moments of small iron clusters: A study based on all-electron DFT, *Solid State Commun.*, 2007, **142**, 114–119.
20 G. Mpourmpakis, G. E. Froudakis, A. N. Andriotis and M. Menon, Role of Co in enhancing the magnetism of small Fe clusters, *Phys. Rev. B: Condens. Matter Mater. Phys.*, 2005, **72**(10), 104417.
21 G. H. Guvelioglu, P. Ma, X. He, R. C. Forrey and H. Cheng, First principles studies on the growth of small Cu clusters and the dissociative chemisorption of H_2, *Phys. Rev. B: Condens. Matter Mater. Phys.*, 2006, **73**(15), 155436.
22 F. Montejo-Alvaro, *et al.*, Icosahedral transition metal clusters (M13, M = Fe, Ni, and Cu) adsorbed on graphene quantum dots, a DFT study, *Phys. E*, 2019, **110**, 52–58.
23 Y. Chen, Z. Huang, P. Hu, J. Chen and X. Tang, Improved performance of supported single-atom catalysts via increased surface active sites, *Catal. Commun.*, 2016, **75**, 74–77.
24 S. Wang, *et al.*, Dopants adsorbed as single atoms prevent degradation of catalysts, *Nat. Mater.*, 2004, **3**, 143–146.
25 J. M. Thomas, Z. Saghi and P. L. Gai, Can a Single Atom Serve as the Active Site in Some Heterogeneous Catalysts?, *Top. Catal.*, 2011, **54**, 588–594.
26 Y. Zhu, *et al.*, Single-Atom Iron-Nitrogen Catalytic Site with Graphitic Nitrogen for Efficient Electroreduction of CO2, *ChemistrySelect*, 2020, **5**, 1282–1287.
27 D. Lyu, *et al.*, Ultra-high surface area graphitic Fe-N-C nanospheres with single-atom iron sites as highly efficient non-precious metal bifunctional catalysts towards oxygen redox reactions, *J. Catal.*, 2018, **368**, 279–290.
28 S. An, *et al.*, High-Density Ultra-small Clusters and Single-Atom Fe Sites Embedded in Graphitic Carbon Nitride (g-C3N4) for Highly Efficient Catalytic Advanced Oxidation Processes, *ACS Nano*, 2018, **12**, 9441–9450.
29 H. Zhang, *et al.*, A Graphene-Supported Single-Atom FeN5 Catalytic Site for Efficient Electrochemical CO2 Reduction, *Angew. Chem., Int. Ed.*, 2019, **58**, 14871–14876.
30 X.-F. Yang, *et al.*, Single-Atom Catalysts: A New Frontier in Heterogeneous Catalysis, *Acc. Chem. Res.*, 2013, **46**, 1740–1748.
31 Y. Chen, Z. Huang, Z. Ma, J. Chen and X. Tang, Fabrication, characterization, and stability of supported single-atom catalysts, *Catal. Sci. Technol.*, 2017, **7**, 4250–4258.
32 U. Heiz, A. Sanchez, S. Abbet and W.-D. Schneider, Catalytic Oxidation of Carbon Monoxide on Monodispersed Platinum Clusters: Each Atom Counts, *J. Am. Chem. Soc.*, 1999, **121**, 3214–3217.
33 W. E. Kaden, T. Wu, W. A. Kunkel and S. L. Anderson, Electronic Structure Controls Reactivity of Size-Selected Pd Clusters Adsorbed on TiO2 Surfaces, *Science*, 2009, **326**, 826–829.
34 Y. Lei, *et al.*, Increased Silver Activity for Direct Propylene Epoxidation via Subnanometer Size Effects, *Science*, 2010, **328**, 224–228.
35 S. Abbet, *et al.*, Acetylene Cyclotrimerization on Supported Size-Selected Pdn Clusters (1 < n < 30): One Atom Is Enough!, *J. Am. Chem. Soc.*, 2000, **122**, 3453–3457.
36 H. Haberland, M. Karrais, M. Mall and Y. Thurner, Thin films from energetic cluster impact: A feasibility study, *J. Vac. Sci. Technol.*, 1992, **10**, 3266–3271.
37 M. Gracia-Pinilla, E. Martínez, G. S. Vidaurri and E. Pérez-Tijerina, Deposition of Size-Selected Cu Nanoparticles by Inert Gas Condensation, *Nanoscale Res. Lett.*, 2009, **5**(1), 180.
38 M. J. Martínez-Carreón, *et al.*, Synthesis and structural analysis of gold-palladium alloy nanoparticles using co-sputtering of independent sources, *Mater. Res. Express*, 2019, **6**, 046515.
39 L. G. Silva, *et al.*, Synthesis of Fe Nanoparticles Functionalized with Oleic Acid Synthesized by Inert Gas Condensation, *J. Nanomater.*, 2014, **2014**, 1–6.
40 M. Gracia-Pinilla, D. Ferrer, S. Mejía-Rosales and E. Pérez-Tijerina, Size-Selected Ag Nanoparticles with Five-Fold Symmetry, *Nanoscale Res. Lett.*, 2009, **4**(8), 896.

41 E. Pérez-Tijerina, *et al.*, Highly size-controlled synthesis of Au/Pd nanoparticles by inert-gas condensation, *Faraday Discuss.*, 2008, **138**, 353–362.
42 Y. Chen, Z. Huang, Z. Ma, J. Chen and X. Tang, Fabrication, characterization, and stability of supported single-atom catalysts, *Catal.: Sci. Technol.*, 2017, **7**, 4250–4258.
43 B. Singh, *et al.*, Single-Atom (Iron-Based) Catalysts: Synthesis and Applications, *Chem. Rev.*, 2021, **121**, 13620–13697.
44 L. Takele Menisa, *et al.*, Single atomic Fe-N4 active sites and neighboring graphitic nitrogen for efficient and stable electrochemical CO2 reduction, *Nanoscale Horiz.*, 2022, **7**, 916–923.
45 Y. Zhu, *et al.*, Single-Atom Iron-Nitrogen Catalytic Site with Graphitic Nitrogen for Efficient Electroreduction of CO2, *ChemistrySelect*, 2020, **5**, 1282–1287.
46 D. Lyu, *et al.*, Ultra-high surface area graphitic Fe-N-C nanospheres with single-atom iron sites as highly efficient non-precious metal bifunctional catalysts towards oxygen redox reactions, *J. Catal.*, 2018, **368**, 279–290.
47 S. An, *et al.*, High-Density Ultra-small Clusters and Single-Atom Fe Sites Embedded in Graphitic Carbon Nitride (g-C3N4) for Highly Efficient Catalytic Advanced Oxidation Processes, *ACS Nano*, 2018, **12**, 9441–9450.
48 H. Zhang, *et al.*, A Graphene-Supported Single-Atom FeN5 Catalytic Site for Efficient Electrochemical CO2 Reduction, *Angew. Chem., Int. Ed.*, 2019, **58**, 14871–14876.
49 H.-J. Shin, *et al.*, Control of Electronic Structure of Graphene by Various Dopants and Their Effects on a Nanogenerator, *J. Am. Chem. Soc.*, 2010, **132**, 15603–15609.
50 B. Kumar, *et al.*, Controlled Growth of Semiconducting Nanowire, Nanowall, and Hybrid Nanostructures on Graphene for Piezoelectric Nanogenerators, *ACS Nano*, 2011, **5**, 4197–4204.
51 H. N. Fernandez-Escamilla, *et al.*, Understanding the Selectivity of the Oxygen Reduction Reaction at the Atomistic Level on Nitrogen-Doped Graphitic Carbon Materials, *Adv. Energy Mater.*, 2021, **11**, 2002459.
52 L. A. Alvarado-Leal, *et al.*, Density Functional Theory Study of Single-Atom Transition Metal Catalysts Supported on Pyridine-Substituted Graphene Nanosheets for Oxygen Reduction Reaction, *ACS Appl. Nano Mater.*, 2023, **7**, 338–347.
53 B. F. Habenicht, D. Teng, L. Semidey-Flecha, D. S. Sholl and Y. Xu, Adsorption and Diffusion of 4d and 5d Transition Metal Adatoms on Graphene/Ru(0001) and the Implications for Cluster Nucleation, *Top. Catal.*, 2013, **57**, 69–79.
54 J. Barth, Transport of adsorbates at metal surfaces: from thermal migration to hot precursors, *Surf. Sci. Rep.*, 2000, **40**, 75–149.
55 B. Han and F. Li, Regulating the electrocatalytic performance for nitrogen reduction reaction by tuning the N contents in Fe3@N_xC20-x (x = 0 4): a DFT exploration, *J. Mater. Inf.*, 2023, **3**(4), 24.
56 M. E. Geusic, M. D. Morse and R. E. Smalley, Hydrogen chemisorption on transition metal clusters, *J. Chem. Phys.*, 1985, **82**, 590–591.
57 K. Yam, N. Guo, Z. Jiang, S. Li and C. Zhang, Graphene-Based Heterogeneous Catalysis: Role of Graphene, *Catalysts*, 2020, **10**, 53.
58 L. Zhang, Q. Xu, J. Niu and Z. Xia, Role of lattice defects in catalytic activities of graphene clusters for fuel cells, *Phys. Chem. Chem. Phys.*, 2015, **17**, 16733–16743.
59 P. Giannozzi, *et al.*, QUANTUM ESPRESSO: a modular and open-source software project for quantum simulations of materials, *J. Phys.: Condens. Matter*, 2009, **21**, 395502.
60 P. Hohenberg and W. Kohn, Inhomogeneous Electron Gas, *Phys. Rev.*, 1964, **136**, B864–B871.
61 W. Kohn and L. J. Sham, Self-Consistent Equations Including Exchange and Correlation Effects, *Phys. Rev.*, 1965, **140**, A1133–A1138.
62 J. P. Perdew, K. Burke and M. Ernzerhof, Generalized Gradient Approximation Made Simple, *Phys. Rev. Lett.*, 1996, **77**, 3865–3868.
63 S. Grimme, J. Antony, S. Ehrlich and H. Krieg, A consistent and accurate ab initio parametrization of density functional dispersion correction (DFT-D) for the 94 elements H-Pu, *J. Chem. Phys.*, 2010, **132**, 154104.
64 H. J. Monkhorst and J. D. Pack, Special points for Brillouin-zone integrations, *Phys. Rev. B: Solid State*, 1976, **13**, 5188–5192.
65 K. S. Novoselov, *et al.*, Electric Field Effect in Atomically Thin Carbon Films, *Science*, 2004, **306**, 666–669.
66 G. Henkelman, A. Arnaldsson and H. Jónsson, A fast and robust algorithm for Bader decomposition of charge density, *Comput. Mater. Sci.*, 2006, **36**, 354–360.
67 M. Yu and D. R. Trinkle, Accurate and efficient algorithm for Bader charge integration, *J. Chem. Phys.*, 2011, **134**(6), 064111.
68 C. Jin, *et al.*, Adsorption of Transition-Metal Clusters on Graphene and N-Doped Graphene: A DFT Study, *Langmuir*, 2022, **38**, 3694–3710.